

NUMERICAL STUDY OF COMBUSTION PROCESSES IN AFTERBURNERS

Zhou Xiaoqing
Chinese Aeronautical Establishment
Beijing, People's Republic of China

and

Zhang Xiaochun
Shenyang Aeroengine Research Institute
Shenyang, People's Republic of China

Mathematical models and numerical methods are presented for computer modeling of aeroengine afterburners. A computer code GEMCHIP is described briefly. The algorithms SIMPLER, for gas flow predictions, and DROPLET, for droplet flow calculations, are incorporated in this code. The block correction technique is adopted to facilitate convergence. The method of handling irregular shapes of combustors and flameholders is described. The predicted results for a low-bypass-ratio turbofan afterburner in the cases of gaseous combustion and multiphase spray combustion are provided and analyzed, and engineering guides for afterburner optimization are presented.

INTRODUCTION

Thus far the design and development of air-breathing engine combustors have been based mainly on ad hoc tests. But the past 10 years have seen a boom of numerical fluid mechanics and combustion. The computer modeling technique is beginning to establish itself in territory which has been dominated exclusively by the empirical technique. It is believed that the combination of numerical modeling with the semi-empirical method and the modern diagnostic technology will greatly promote combustion study and combustor design and development.

The objective of this paper (which is part of the authors' continuing effort to make computer models of multiphase turbulent combustion processes in combustors and furnaces (refs. 1 and 2 and private communication with X. Zhang and H.H. Chiu, University of Illinois at Chicago, 1984)) is to present mathematical models and numerical methods for combustor flows and to apply these methods to the computer prediction of aeroengine afterburner characteristics.

The long-ignored droplet-turbulent-diffusion model plays an important role in droplet dispersion and species distribution. It has now been incorporated in this modeling. The $K-\epsilon$ turbulence model is modified and extended to account for multiphase turbulence effects. A hybrid, finite-rate chemical-reaction model based on a global Arrhenius law and a turbulent mixing-rate model is used judiciously to predict the combustion rate of multiphase premixed turbulent flames. A system of conservation equations of the Eulerian type is used for both gaseous flow and multisized droplet flow predictions. To solve these equations, the authors developed a computer code called GEMCHIP (general, elliptic-type, multiphase, combustion-heat-transfer, and interdiffusion program), in which the SIMPLER algorithm (ref. 3) for gaseous flow prediction

and the DROPLET (private communication with X. Zhou and H.H. Chiu, University of Illinois at Chicago, 1983) procedure for droplet flow calculation were incorporated. The block correction technique and the alternating-direction reciprocating-sweep line-by-line TDMA (tri-diagonal matrix algorithm) method was adopted to facilitate convergence of the iteration processes.

The afterburner under study is a low-bypass-ratio turbofan engine augmentor of the axisymmetric type with a bluff body flameholder. The method of simulating the irregularly shaped flow domain and the flameholder configuration is described briefly and the inlet and boundary conditions are presented. The usual wall functions (ref. 4) are used to bridge the near wall regions where local Reynolds numbers are very low.

The numerical results of gas flow, droplet flow fields, and the spray flame structures are presented. A study of the parametric sensitivity of the combustion efficiency is made for both gas combustion and multiphase combustion. Engineering guides are given for afterburner design optimization.

SYMBOLS

C_p	specific heat of gas at constant pressure
E	activation energy
h	total enthalpy
J	work-heat equivalence
K	turbulent kinetic energy
L	latent heat of vaporization
P	gas pressure
q	heat value of fuel
R_u	universal gas constant
r_d	droplet radius
T	temperature
U, V	velocities in X and R directions, respectively
W	molecular weight
Y	species mass concentration
Γ	gamma function; transport coefficient
γ	stoichiometric coefficient

ξ turbulence dissipation rate

λ heat conductivity

μ viscosity

ρ density

Φ mixture fraction

Nondimensional numbers:

D_1 first Damkohler number

Ec Eckert number

Eu Eulerian number

G_C spray group combustion number

G_d spray group aerodynamic drag number

G_v spray group droplet preheating number

L_{mk} mass fraction of liquid in the mixture

Nu Nusselt number

Pe Peclet number

Pr Prandtl number

Re Reynolds number

Sc Schmidt number

τ_{TR} ratio of flow residence time to turbulence dissipation time

ϵ_R ratio of turbulent kinetic energy to mean flow value

σ turbulent Schmidt/Prandtl number

Subscripts:

b boiling point

eff effective

F fuel

g gas

k Kth size group of droplets

l liquid

M,m mean
o initial or inlet condition
ox oxygen
p product
T,t turbulent; temperature

MATHEMATICAL FORMULATION

The Eulerian scheme is used to construct elliptic-type conservation equations for both gaseous and droplet phases in two-dimensional, multiphase, combusting, turbulent flows. Nondimensionalization of these equations leads to the following two general forms (ref. 1 and private communication with X. Zhou and H.H. Chiu, University of Illinois at Chicago, 1983):

$$\frac{1}{\bar{r}^i} \left[\frac{\partial}{\partial \bar{x}} \left(\bar{r}^i \bar{f}_x \bar{\xi} - \bar{r}^i \Gamma_{\xi} \frac{\partial \bar{\xi}}{\partial \bar{x}} \right) + \frac{\partial}{\partial \bar{r}} \left(\bar{r}^i \bar{f}_r \bar{\xi} - \bar{r}^i \Gamma_{\xi} \frac{\partial \bar{\xi}}{\partial \bar{r}} \right) \right] = S_{\xi} + S_{int} \quad (1)$$

$$\frac{1}{\bar{r}^i} \left[\frac{\partial}{\partial \bar{x}} (\bar{r}^i \bar{f}_x \bar{\xi}) + \frac{\partial}{\partial \bar{r}} (\bar{r}^i \bar{f}_r \bar{\xi}) \right] - \frac{\bar{\xi}}{\bar{r}^i} \left[\frac{\partial}{\partial \bar{x}} (\bar{r}^i \bar{f}_x) + \frac{\partial}{\partial \bar{r}} (\bar{r}^i \bar{f}_r) \right] = S_{int} \quad (2)$$

where \bar{f}_x and \bar{f}_r are fluxes in the X and R directions, respectively; Γ_{ξ} is the transport coefficient for the variable ξ , S_{ξ} and S_{int} are the inner-phase and interphase source terms, respectively, and i takes the values $i = 1$ for the cylindrical coordinate and $i = 0$ for the Cartesian coordinate.

All conservation equations in these two forms are summarized in tables I and II, respectively.

The physical models employed or developed in this study are introduced in the following sections.

Spray Spectrum Model

The generalized Rosin-Rammler function is adopted to derive the size derivative of the droplet number density:

$$f_{n,l} = \frac{n_l S}{r_{l,m} \Gamma} \frac{\Gamma [(t+4)/S]^{(t+1)/3}}{\Gamma [(t+1)/S]^{(t+4)/3}} \left(\frac{r_l}{r_{l,m}} \right)^t \exp \left\{ - \left(\frac{r_l}{r_{l,m}} \right)^S \left[\frac{\Gamma [(t+4)/S]}{\Gamma [(t+1)/S]} \right]^{S/3} \right\} \quad (3)$$

$$n_{l,k} = \int_{r_{l,k-1/2}}^{r_{l,k+1/2}} f_{n,l} dr_l \quad (4)$$

where S and t characterize the spray spectrum quality, Γ denotes gamma function, and n_l and $r_{l,m}$ are the droplet number density and the volume-mean initial droplet radius.

DROPLET Turbulent Diffusion Model

Besides the trajectory motion, droplets also disperse through diffusion caused by the gas turbulence. A droplet diffusion model is formulated (private communication with X. Zhou and H.H. Chiu, University of Illinois at Chicago, 1983 and ref. 5) which takes the following final forms:

$$\sigma_{nl} = \psi \sigma_g \quad (5)$$

$$\psi = \left[1 + \sum_j^3 h_j \left(\frac{\rho_l}{\rho_g} \frac{\epsilon}{K} - r_l^2 \right)^j \right] \quad (6)$$

$$\overline{n_l \vec{v}_l} = - \frac{\mu_T}{\rho_g \sigma_g} \nabla n_l \quad (7)$$

$$\overline{n_l \vec{v}_l} = - \frac{\mu_T}{\rho_g \sigma_{nl}} \nabla n_l \quad (8)$$

where σ_g and σ_{nl} are the gas and droplet turbulent Schmidt numbers, respectively.

Modified K- ϵ Model

The original K- ϵ turbulence model is modified to take account of droplet-phase effects. The droplets are assumed to share turbulent kinetic energy with the gas phase. The relationship of turbulent kinetic energies between gas and droplets can be approximated as

$$K_l \sim K/\psi^2$$

The modified K-equation is expressed as

$$\nabla \cdot (\theta \rho_g \vec{v}_g K) = \nabla \cdot \left(\theta \frac{\mu_{eff}}{\sigma_K} \nabla K \right) + \theta G_K - \theta \rho_g \epsilon - \nabla \cdot \int_0^{\dot{m}_l} K_l \vec{v}_l d\dot{m}_l \quad (9)$$

The ϵ -equation remains unchanged.

Hybrid Turbulent Gas Combustion Model

The combustion reaction is supposed to take place in a single step:



A hybrid combustion model is adopted; it assumes that the combustion rate is controlled by the slower of two competitive rates of successive subprocesses - the chemical reaction rate and the turbulent mixing rate. The former rate is determined by the Arrhenius law, the latter rate is calculated from the eddy-break-up (EBU) model

$$R_F = - \min \left(|R_{F,EBU}|, |R_{F,Ar}| \right) \quad (11)$$

where

$$R_{F,EBU} = -C_R \theta \rho_g K^{1/2} \left[\left(\frac{\partial Y_F}{\partial X_1} \right)^2 + 1 \left(\frac{\partial Y_F}{\partial X_2} \right)^2 + \left(\frac{\partial Y_F}{\partial X_3} \right)^2 \right]^{1/2}$$

$$R_{F,Ar} = -B_a T_g^\alpha \rho_g^2 Y_F Y_{Ox} \exp (-E/R_u T_g)$$

NUMERICAL METHODS

A 42 by 38 staggered grid system is superimposed on the flow domain. The previously mentioned two general forms of nonlinear partial differential equations are then discretized into their finite difference counterparts by using the control volume scheme and the primitive variables of pressure and velocity. The power law scheme (ref. 3) is adopted to determine combined diffusion/convection fluxes. The SIMPLER procedure is employed to predict gaseous flow fields, it reduces computer time by 30 to 50 percent in comparison with the popular SIMPLE procedure. The DROPLET procedure is used for calculating droplet flow fields. The alternating-direction double-reciprocating-sweep line-by-line TDMA method is adopted to solve simultaneous algebraic equations iteratively. The block correction technique is used to facilitate convergence. The usual wall function method is employed to bridge the near wall regions where the laminar viscosity effect is quite strong. This method is very effective in greatly reducing computer time while obtaining rather satisfactory results. All these methods have been assembled into the computer code GEMCHIP. The main flow chart of GEMCHIP is shown in figure 1.

A droplet-free solution is first obtained through SIMPLER, which provides both final results for the single gas-phase flow and the initial guesses of the gas flow fields for multiphase flow. Then we enter DROPLET to calculate droplet flow fields and the interphase exchanges of mass, momentum, and energy. These quantities are substituted as source terms into SIMPLER, and the gas flow fields are modified. Then we enter DROPLET again. This alternating iterative process continues until all the gas- and droplet-flow equations satisfy the convergence criterion in all grids. The typical iteration number ranges from 40 to 75 for gas-phase burning problems and from 120 to 150 for multiphase burning problems. The corresponding computer times are about 5 and 30 min, respectively, on an IBM 4342 machine.

THE AFTERBURNER STUDIED

Figure 2 shows a low-bypass-ratio turbofan afterburner in which the computer modeling is made. The afterburner consists of a cone-type diffuser/mixer, a cylindrical combustion section, and a single-ring bluff-body flameholder. A cylindrical partition board separates the cold fan flow from the hot core flow. The temperature and velocity are 350 K and 80 m/sec in the fan flow and 600 to 800 K and 60 to 200 m/sec in the core flow. The liquid fuel is evenly injected in spray form into the core flow, and then the droplets are heated, vaporized, mixed, and combusted with oxygen in the airflow.

Handling of Irregularly Shaped Wall and Flameholder

The curved afterburner wall and the flameholder are simulated by blocking off some of the control volumes of the regular grid system so that the remaining active control volumes form the desired shape. The advantage of this method is that a computer code developed for the nominally regular domain can be adapted to flows of arbitrarily shaped configurations so that there is no need to generate new programs and the time for developing and testing such programs is saved.

The irregular boundary can be represented approximately by a series of rectangular steps (fig. 3). Usually a rather crude representation of the boundary can produce surprisingly good results.

The values of the relevant flow parameters should be given in the blocked-off regions. This is done by using extremely large source terms or by assigning extremely large transport coefficients in these inactive control volumes. These inactive grids also participate in the iteration process.

Boundary Conditions

Appropriate boundary conditions are selected to represent the wall regions of the afterburner. The following assumptions can be realistically made with regard to this kind of selection:

- (1) No slip at the wall
- (2) Zero turbulent fluctuation at the wall
- (3) Adiabatic and impermeable wall

It is reported that the predicted solution is very sensitive to the inlet conditions. For this reason, the inlet profiles should conform to measured values whenever available. Unfortunately, measurements of the profiles of the inlet variables, especially the inlet velocity vectors and the inlet turbulence variables K and ϵ , are seldom carried out in complex geometries. It is, therefore, reasonable to assume the following profiles (ref. 6):

$$U_g = U_{g0}(1 - \bar{r})^n$$

$$V_g = 0$$

$$K = K_0 (1 + m(\bar{r})^2)$$

$$\epsilon = \epsilon_0 (K/K_0)^{1.5}$$

where $0.2 \geq n \geq 0$ and $2 \geq m \geq 0$. The variables with subscript o denote values at the centers of core flow or fan flow. The nondimensional radius $\bar{r} = r/R$ for the core flow and $\bar{r} = |r - (R_1 + R_0)/2|/((R_1 + R_0)/2)$ for the fan flow, where R_0 denotes the radius of the partition board and R_1 represents the diffuser's inlet radius.

The inlet profiles of the droplet number densities, temperatures, and velocities vary with the fuel nozzle type and spray quality.

In the axis of symmetry the radial gradients of all droplet-phase variables are taken to be equal to zero.

The exit plane should be located far downstream and outside the recirculation zone so that the local parabolic flow assumption applies and that the calculating domain is isolated from the ambient environment. The only exceptions are the equations for pressure p and for the pressure correction parameter p' , since the pressure effect is always two way. The problem is solved by calculating the outlet velocity component in the main flow direction.

RESULTS AND DISCUSSIONS

The objectives of the numerical study are to analyze the shape and the size of recirculation zones at different working conditions, to examine the vaporization process of multisize fuel sprays, to compare the multiphase flame structures with the gas flame structures, and to study the parametric sensitivity of afterburning efficiency.

Recirculation Zones

The gas velocity vector fields inside the afterburner are shown in figures 4 to 6 for gas flow and multiphase flow. The numerical calculations reveal that the recirculation zones in the wake of the flameholder are induced by negative pressure gradients, which, in turn, are caused by gaseous viscosity.

Figures 4 and 5 are pictures of velocity vectors and X-direction velocity component profiles in a gas phase flow. The length of the recirculation zone in the cold flow case is about 2.0 to 3.5 times the flameholder width. It is readily seen from figure 4 and 5 that the wake effect still exists far downstream of the flameholder. Some experimental reports claim that the recirculation zone will become larger and longer in gas combustion cases because of gas expansion and the reduction of the absolute value of the negative pressure behind the flameholder. But this trend is not obvious in this calculation. Research work is under way in this direction.

Figure 7 shows droplet velocity vectors of two size groups in the multiphase afterburning condition. A comparison of the multiphase flow with the gas flow field (fig. 6) shows that the small droplets are capable of reaching

velocity equilibrium more quickly than the large droplets. The velocity non-equilibrium in the downstream is somewhat enhanced because the gas is accelerated more rapidly than the droplets. This is especially true for the large droplets. The droplet recirculation zone is obviously smaller than the gas recirculation zone.

Cascading Vaporization

The preheating and vaporization processes of droplets of different size groups are illustrated in figure 8. It is readily seen from the predicted curves that the small droplets (e.g., $\bar{D}_1 = 0.15$) complete the preheating process and initiate the vaporization process much earlier than the large droplets (e.g., $\bar{D}_1 = 1.60$).

The phenomenon of successive initiation of the vaporization of droplets of different sizes in spray is designated as cascading vaporization (ref. 1) since the initial vaporization lines of different size droplets constitute a form of cascade.

Gas Flame and Multiphase Flame Structures

Figures 9(a) and (b) show the temperature field and flame structure of the gas combustion flow. The gas flame structure is rather simple: the flow of the combustible mixture mixes with the fan flow of the cold air, and the flame is stabilized in the recirculation zone close behind the flameholder. There is a "dark" area, which is fuel-deficient, in the wake of the flameholder. This is where the combustion is completed.

The structure of the multiphase flame is very complicated. Calculation reveals that there are three principal combustion modes: (1) pre-evaporating flame, (2) dense spray group flame, and (3) dilute spray group flame. The total fuel-air ratio and the spray group combustion number G_c are the two main parameters determining combustion mode. The G_c is actually the ratio of the characteristic vaporization rate to the convection flow rate and was first proposed by Prof. H.H. Chiu (ref. 7).

Pre-evaporating flame. - The pre-evaporation flame is shown in figure 10. When the G_c number is very large (fine atomization, i.e., the spray consists of an extremely large quantity of small droplets) all the droplets are vaporized at a typical afterburner inlet temperature before they get to the flame zone. The flame structure is similar to that of gas phase combustion.

Dense spray group flame. - If the G_c number is rather large and the fuel-air ratio is also high, dense spray group combustion occurs (fig. 11); this is characterized by the presence of an oxygen-deficient zone, which decreases combustion efficiency. Both types of gas and droplet burning coexist in the flame.

Dilute spray group flame. - This mode occurs at a small G_c number, which is characterized by poor atomization quality and a low fuel-air ratio: that is, there is a small quantity of big droplets. If the droplet size is large enough and droplets concentrate near the central line of the afterburner, the v-type flame shown in figure 12 may appear. This type of flame is unstable.

Figures 13(a) and (b) show, respectively, the axial distributions of afterburning efficiencies in gas-phase and multiphase combustion cases. It is seen that the growth of the combustion efficiency for the multiphase flame has a slower start than that for the gas flame. This difference is caused by the droplet preheating and by vaporization processes. The results also indicate that the smaller the spray group combustion number G_c , the larger the difference.

Parametric Sensitivity Study of Combustion Efficiency

Figure 14 shows the effect of fuel-air ratio on gas-phase combustion efficiency at two different pressures (2.0 kg/cm^2 and 0.5 kg/cm^2). The efficiency curve reaches its peak at an approximately stoichiometric fuel-air ratio in the core flow. At higher pressures, the efficiency peak moves toward richer mixtures and the curve becomes flatter because of the dilution action by the fan flow and the improvement of combustion conditions.

Figure 15 shows the variation of the multiphase combustion efficiency with the fuel-air ratio at two different spray group combustion numbers. With multiphase combustion there is a combustion efficiency peak at an appropriate fuel-air ratio similar to that with gas-phase combustion. With an increase of G_c number, the efficiency peak moves toward leaner mixtures - which means mixtures with a larger number of smaller-sized droplets will have a higher combustion efficiency at a lower fuel-air ratio. The results are also in agreement with the experimental measurements.

Figures 16(a) and (b) show the effect of the inlet gas temperature on combustion efficiencies of gas-phase and multiphase flames. The temperature increase enhances the heat release rate and speeds up droplet vaporization, which, in turn, enhances the combustion efficiencies of both the gas and multiphase flames. But, for obvious reasons, the temperature effect is stronger in multiphase flames.

The effect of inlet gas pressure on combustion efficiency is similar to that of inlet temperature. It is seen from figure 14 that, in the case of gas phase combustion, an increase of gas pressure from 0.5 to 2.0 kg/cm^2 significantly improves combustion. Figure 17 shows the increase of combustion efficiency with gas pressure in a multiphase combustion case. The pressure effect is negligible at pressures greater than 1.3 kg/cm^2 .

Figure 18 shows the effect of gas-flow velocity on gas-phase combustion efficiency. An increase in gas velocity results in a decrease in combustion efficiency because of the reduction of the residence time of the gas flow in the afterburner. The higher the velocity, the lower the efficiency. The effect of inlet gas velocity on multiphase combustion efficiency is rather complicated since the velocity affects not only the residence time but also the droplet atomization, vaporization, and spray group combustion number G_c .

CONCLUSIONS

The mathematical models and numerical methods for predicting multiphase turbulent reacting flows, developed in the authors' study of spray group combustion phenomena have been successfully extended and applied to the numerical

study of flow fields and combustion characteristics of a low-bypass-ratio turbofan afterburner. The computer code developed by the authors is versatile and effective in this study. The technique of blocking off relevant control volumes makes it possible for a computer code developed for a regular grid system to be applied to arbitrary flow domains.

The numerical analysis reveals that the size of the recirculation zone behind the flameholder is about 2.0 to 3.5 times its width. The droplet recirculation zone is smaller than the gas recirculation zone and decreases or even disappears with an increase in droplet size.

The calculation also exposes the existence of three principal combustion modes in multiphase combustion. They are the pre-evaporating flame mode, the dense spray group flame mode, and the dilute spray group flame mode. Study of flame structure is useful to afterburner design optimization.

The results reveal the dependence of afterburner combustion efficiency on the fuel-air ratio and on the operating parameters (such as the inlet gas temperature, pressure, and velocity). As for multiphase combustion, which prevails in turbofan afterburners, the spray group combustion number has a significant effect on combustion efficiency and flame structure. It is concluded that afterburners should be designed to work in the optimum spray group combustion number, which is related to the fuel-air ratio and its distribution. Generally speaking, the favorable design has a pre-evaporating flame mode or a dense group combustion mode with an initial fuel distribution capable of keeping oxygen-deficient zones as small as possible.

Although the previously predicted results are in good qualitative agreement with the known facts, accurate diagnostic measurements and detailed experimental verifications are necessary to examine the quantitative agreement and to improve the present models.

REFERENCES

1. Chiu, H.H.; and Zhou, Xiaoqing: Turbulent Spray Group Evaporation and Combustion, 9th International Colloquium on Dynamics of Explosion and Reactive System, Poitier, France, 1983.
2. Zhou, Xiaoqing; and Chiu, H.H.: Spray Group Combustion Processes in Air Breathing Propulsion Combustors, AIAA-83-1323, AIAA/ASME/SAE 19th Joint Propulsion Conference, 1983, Seattle, U.S.A.
3. Patankar, S.V.: Numerical Heat Transfer and Fluid Flow, McGraw-Hill, 1980, U.S.A.
4. Launder, B.E.; and Spalding, D.B.: The Numerical Computation of Turbulent Flows, Computer Method in Applied Mechanics and Engineering, Vol. 3, pp. 269-289, 1974.
5. Ward, P.; Collings, N.; and Hay, N.: A Comparison of Simple Models of Turbulent Droplet Diffusion Suitable for Use in Computations of Spray Flames, ASME-82-WA/HT-2.

6. Khalil, E.E.: Numerical Computations of Turbulent Reacting Combustion Flows, Numerical Method in Heat Transfer, 1981, John Wiley and Sons Ltd.
7. Chiu, H.H.; and Liu, T.M.: Group Combustion of Liquid Droplets, Combustion Science and Technology, 1977, Vol. 17, pp. 127-142.

TABLE I. - THE GOVERNING EQUATIONS IN THE FORM OF EQUATION (1)

(a) Form of equation (1)

Type of equation	\bar{r}_x	\bar{r}_r	$\bar{\xi}$	\bar{r}_ξ	S_ξ	S_{Int}
Continuity	$\bar{\rho}_g \bar{U}_g$	$\bar{\rho}_g \bar{V}_g$	1	0	0	$-\frac{6_c \bar{\lambda}}{3} \sum_{k=1}^M \bar{r}_{g,k}^{-3} \frac{\partial}{\partial \bar{r}_{g,k}} \left(\frac{\bar{n}_{g,k}}{\bar{r}_{g,k}} \bar{U}_{g,k} \bar{\phi}_{r,k} \right)$
Gas phase X-direction momentum	$\bar{\rho}_g \bar{U}_g$	$\bar{\rho}_g \bar{V}_g$	\bar{U}_g	$\frac{2}{Re_0} \bar{\nu}_{eff}$	$-\frac{Eu}{\theta_0} \frac{\partial \bar{p}}{\partial \bar{x}} + Re_0 \left[\frac{\partial}{\partial \bar{x}} \left\{ \frac{2}{3} \bar{\nu}_{eff} \left(\frac{\partial \bar{U}_g}{\partial \bar{x}} + \frac{1}{\bar{r}_1} \frac{\partial}{\partial \bar{r}} \left(\bar{r}_1 \bar{\nu}_{eff} \frac{\partial \bar{U}_g}{\partial \bar{x}} \right) \right\} + \bar{\nu}_{eff} \frac{\partial \bar{U}_g}{\partial \bar{x}} \right] + \frac{\partial}{\partial \bar{r}} \left(\bar{r}_1 \bar{\nu}_{eff} \frac{\partial \bar{U}_g}{\partial \bar{x}} \right)$	$-\frac{6_c \bar{\lambda}}{3} \sum_{k=1}^M \bar{r}_{g,k}^3 \bar{U}_{g,k} \frac{\partial}{\partial \bar{r}_{g,k}} \left(\frac{\bar{n}_{g,k}}{\bar{r}_{g,k}} \bar{U}_{g,k} \bar{\phi}_{r,k} \right) - \bar{G}_d \cdot \sum_{k=1}^M \frac{\bar{Z}_g}{1 + \bar{B}_k} \bar{\nu}_{eff} \bar{r}_{g,k} (\bar{U}_g - \bar{U}_{g,k})$
Gas phase R-direction momentum	$\bar{\rho}_g \bar{U}_g$	$\bar{\rho}_g \bar{V}_g$	\bar{V}_g	$\frac{2}{Re_0} \bar{\nu}_{eff}$	$-\frac{Eu}{\theta_0} \frac{\partial \bar{p}}{\partial \bar{r}} + Re_0 \left[\frac{\partial}{\partial \bar{x}} \left(\bar{\nu}_{eff} \frac{\partial \bar{U}_g}{\partial \bar{x}} \right) + \frac{\partial}{\partial \bar{r}} \left(\bar{r}_1 \bar{\nu}_{eff} \frac{\partial \bar{U}_g}{\partial \bar{x}} \right) \right] + \frac{\partial}{\partial \bar{r}} \left(\bar{r}_1 \bar{\nu}_{eff} \frac{\partial \bar{U}_g}{\partial \bar{x}} \right)$	$-\frac{6_c \bar{\lambda}}{3} \sum_{k=1}^M \bar{r}_{g,k}^3 \bar{V}_{g,k} \frac{\partial}{\partial \bar{r}_{g,k}} \left(\frac{\bar{n}_{g,k}}{\bar{r}_{g,k}} \bar{U}_{g,k} \bar{\phi}_{r,k} \right) - \bar{G}_d \sum_{k=1}^M \frac{\bar{Z}_g}{1 + \bar{B}_k} \bar{\nu}_{eff} \bar{r}_{g,k} (\bar{V}_g - \bar{V}_{g,k})$
Gas fuel conservation	$\bar{\rho}_g \bar{U}_g$	$\bar{\rho}_g \bar{V}_g$	γ_f	$\frac{2\theta}{Re} \frac{\bar{\nu}_{eff}}{\sigma_f}$	(1) Arrhenius Law $-\bar{D}_1 \bar{\theta}_f^{\alpha-2} \rho_g \gamma_{f,ox} \exp \left[-\frac{E}{RT_0} \left(\frac{1}{T_g} - 1 \right) \right]$ (2) EBU model $-C_{R,R}^{1/2} \bar{\theta}_f^{\alpha-1/2} \bar{K}_g^{1/2} \left[\left(\frac{\partial \gamma_f}{\partial \bar{x}} \right)^2 + \left(\frac{\partial \gamma_f}{\partial \bar{r}} \right)^2 \right]^{1/2}$	$-\frac{6_c \bar{\lambda}}{3} \sum_{k=1}^M \bar{r}_{g,k}^{-3} \frac{\partial}{\partial \bar{r}_{g,k}} \left(\frac{\bar{n}_{g,k}}{\bar{r}_{g,k}} \bar{U}_{g,k} \bar{\phi}_{r,k} \right)$
Mixture fraction conservation	$\bar{\rho}_g \bar{U}_g$	$\bar{\rho}_g \bar{V}_g$	ϕ	$\frac{2\theta}{Re} \frac{\bar{\nu}_{eff}}{\sigma_\phi}$	0	$-\frac{6_c \bar{\lambda}}{3} \sum_{k=1}^M \bar{r}_{g,k}^{-3} \frac{\partial}{\partial \bar{r}_{g,k}} \left(\frac{\bar{n}_{g,k}}{\bar{r}_{g,k}} \bar{U}_{g,k} \bar{\phi}_{r,k} \right)$

TABLE I. - Continued.

Gas energy conservation	$\bar{\theta} \rho_g \bar{U}_g$	$\bar{\theta} \rho_g \bar{V}_g$	\bar{h}	$\frac{2\bar{\theta}}{\text{Re}} \frac{\bar{\nu}_{\text{eff}}}{\sigma_h}$	$\frac{Ec_g}{2} \frac{\bar{\theta}}{\text{Re}} \bar{\theta}_{\text{eff}} G_u$ where $G_u = \left[2 \left(\frac{\partial \bar{U}_g}{\partial \bar{x}} \right)^2 + 2 \left(\frac{\partial \bar{V}_g}{\partial \bar{r}} \right)^2 + \right. \\ \left. 2 \left(\frac{\bar{V}_g}{\bar{r}} \right)^2 \delta(1) + \left(\frac{\partial \bar{U}_g}{\partial \bar{r}} + \frac{\partial \bar{V}_g}{\partial \bar{x}} \right)^2 \right]$	$\frac{-G_c \bar{\lambda}}{1 - T_{LO}/T_{g0}} \sum_{k=1}^M \bar{Nu}_{c,k} (T_g - T_{g,k}) \bar{r}_{g,k} \bar{n}_{g,k} \delta(T_{g,k})$ $-\frac{G_c}{3} \left(\frac{U_F}{\omega_F} - 1 \right) \frac{\bar{\lambda}}{C_p} \sum_{k=1}^M \bar{r}_{g,k}^3 \frac{\partial}{\partial \bar{r}_{g,k}} \left(\frac{\bar{n}_{g,k}}{\bar{r}_{g,k}} \bar{Nu}_{g,k} \right)$ $\Phi_{r,k} + G_d Ec_g \sum_{k=1}^M \left\{ \frac{Z \bar{n}_{g,k} \bar{r}_{g,k}}{1 + B_k} \bar{r}_{g,k} \left[(U_g - U_{g,k})^2 + (\bar{V}_g - \bar{V}_{g,k})^2 \right] \right\}$
K-equation	$\bar{\theta} \rho_g \bar{U}_g$	$\bar{\theta} \rho_g \bar{V}_g$	R	$\frac{2\bar{\theta}}{\text{Re}} \frac{\bar{\nu}_{\text{eff}}}{\sigma_k}$	$\frac{2}{\text{Re} c_R} \bar{\theta} \bar{\mu} - G_u - \tau_{TR} \bar{\theta} \rho_g \bar{\epsilon}$	$-L_{mR} \sum_{k=1}^M \bar{r}_{g,k}^3 \frac{1}{\bar{r}_{g,k}} \left[\frac{\partial}{\partial \bar{x}} \left(\bar{r}_{g,k} \bar{n}_{g,k} \bar{U}_{g,k} \right) + \frac{\partial}{\partial \bar{r}} \left(\bar{r}_{g,k} \bar{n}_{g,k} \cdot \bar{V}_{g,k} \bar{r}_{g,k} \right) \right]$
ϵ - Equation	$\bar{\theta} \rho_g \bar{U}_g$	$\bar{\theta} \rho_g \bar{V}_g$	$\bar{\epsilon}$	$\frac{2\bar{\theta}}{\text{Re}} \frac{\bar{\nu}_{\text{eff}}}{\sigma_\epsilon}$	$\frac{C_1 C_u}{\tau_{TR}} \bar{\theta} k \rho_g G_u - C_2 \tau_{TR} \bar{\theta} \rho_g \frac{\bar{\epsilon}^2}{R}$	0
G-Equation*	$\bar{\theta} \rho_g \bar{U}_g$	$\bar{\theta} \rho_g \bar{V}_g$	$\bar{\delta}$	$\frac{2\bar{\theta}}{\text{Re}} \frac{\bar{\nu}_{\text{eff}}}{\sigma_G}$	$C_{g1} \frac{2\bar{\theta} \bar{\mu}_t}{\text{Re} \sigma_G} \left[\left(\frac{\partial \bar{\Phi}}{\partial \bar{x}} \right)^2 + \left(\frac{\partial \bar{\Phi}}{\partial \bar{r}} \right)^2 \right] - C_{g2} \tau_{TR} \cdot \bar{\theta} \rho_g (\bar{\epsilon}/R) \bar{\delta}$	$\frac{G_c}{3} G \frac{\bar{\lambda}}{C_p} \sum_{k=1}^M \bar{r}_{g,k}^3 \frac{\partial}{\partial \bar{r}_{g,k}} \left(\frac{\bar{Nu}_{g,k}}{\bar{r}_{g,k}} \bar{n}_{g,k} \Phi_{r,k} \right)$
Droplet number-density	$\bar{U}_{g,k}$	$\bar{V}_{g,k}$	$\bar{n}_{g,k}$	$\frac{2}{\text{Re}} \frac{\bar{\mu}_t}{\rho_g \sigma_g \psi}$	$\frac{G_c}{3 L_{mR}} \frac{\bar{\lambda}}{C_p} \frac{\partial}{\partial \bar{r}_{g,k}} \left(\frac{\bar{Nu}_{g,k}}{\bar{r}_{g,k}} \bar{n}_{g,k} \Phi_{r,k} \right)$	0

*G-equation used for turbulent diffusion flame; not mentioned in text.

TABLE I. - Concluded.
(b) Form of equation (2)

Type of equation	$\bar{\epsilon}$	$\bar{\epsilon}_x$	$\bar{\epsilon}_r$	S_{int}
X-direction droplet moment	$\bar{U}_{g,k}$	$\bar{n}_{g,k} \bar{U}_{g,k}$	$\bar{n}_{g,k} \bar{V}_{g,k}$	$\frac{G_d}{L_{mR}(1+B_g)} \frac{Z \bar{\mu} \bar{n}_{g,k}}{r^2} (U_g - U_{g,k})$
R-direction droplet moment	$\bar{V}_{g,k}$	$\bar{n}_{g,k} \bar{U}_{g,k}$	$\bar{n}_{g,k} \bar{V}_{g,k}$	$\frac{G_d}{L_{mR}(1+B_g)} \frac{Z \bar{\mu} \bar{n}_{g,k}}{r^2} (V_g - V_{g,k})$
Droplet temperature	$\bar{T}_{g,k}$	$\bar{n}_{g,k} \bar{U}_{g,k}$	$\bar{n}_{g,k} \bar{V}_{g,k}$	$\frac{G_v}{L_{mR}} \frac{C_{p0}}{C_g} \frac{\lambda M U_{c,k} \bar{n}_{g,k}}{r^2} (T_g - T_{g,k})$

where $C_1 = 1.44$, $C_2 = 1.92$, $C_\mu = 0.09$, $C_R = 1.07$, $C_{g1} = 2.8$, $C_{g2} = 2.0$,

$$\sigma_f = \sigma_{ox} = \sigma_\phi = \sigma_h = \sigma_G = 0.7, \sigma_g = 0.9, \sigma_K = 1.0, \sigma_\epsilon = 1.3$$

$$G_c = 4\pi \frac{\lambda_0}{C_{p0}} \frac{n_{g0} r_{gm,0}^2 R_{U_{g,0}}}{\theta_0 \rho_{g0} U_{g,0}} ; G_d = 6\pi \frac{\nu_{g0} r_{gm,0}^2 n_{g,0} Z}{\theta_0 \rho_{g0} U_{g,0}} ; G_v = 4\pi \frac{Nu_{c,0} r_{gm,0}^2 n_{g,0} R_0^2}{\theta_0 Pe} ;$$

$$L_{mR} = \frac{\rho_g}{\rho_0} \frac{1 - \theta_0}{\theta_0} ; \tau_{TR} = \frac{\epsilon_{g0}}{k_0 U_{g0}} ; Pe = 2U_{g0} \frac{R_{c0} \rho_{g0}}{\lambda_0} ; Re = \frac{2U_{g0} R_{c0} \rho_{g0}}{\nu_0} ;$$

$$Eu = \frac{p_{g0}}{\rho_{g0} U_{g0}^2} ; Ec_g = \frac{U_{g0}^2}{J C_{p0} (T_{g0} - T_{g,0})} ; D_1 = \frac{R_0}{U_{g0}} \frac{B_1 T_{g,0}^2}{a_0 \rho_{g0} w_{ox}} \frac{1}{\exp \frac{-E}{R_{U,0}}} ;$$

$$Re_m = \frac{2U_{g0} r_{gm,0} \rho_{g0}}{\nu_0} ; \epsilon_R = \frac{K_0}{U_{g0}^2}$$

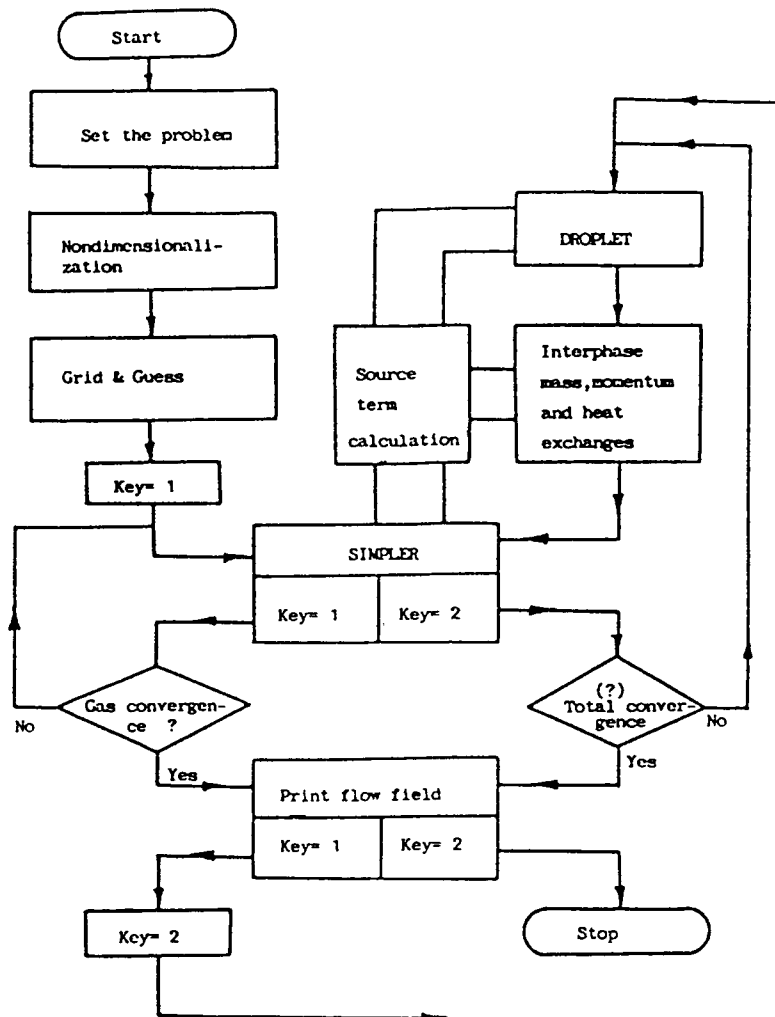


Figure 1. - Main flowchart of GEMCHIP.

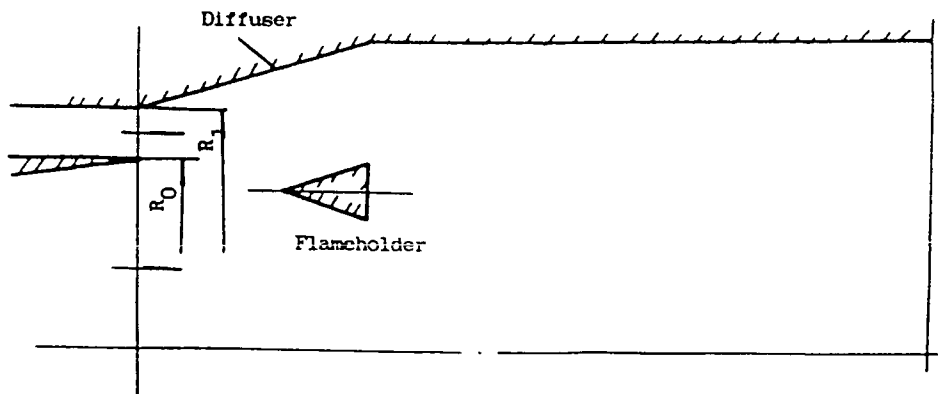


Figure 2. - Afterburner studied.

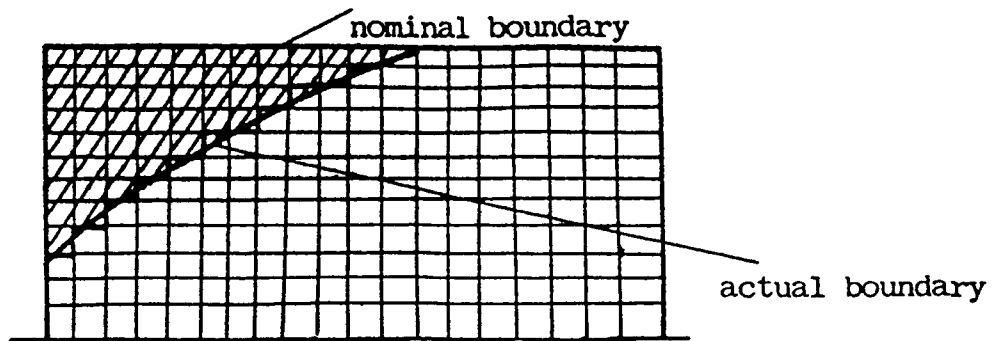


Figure 3. - Blocked-off region in regular grid system.

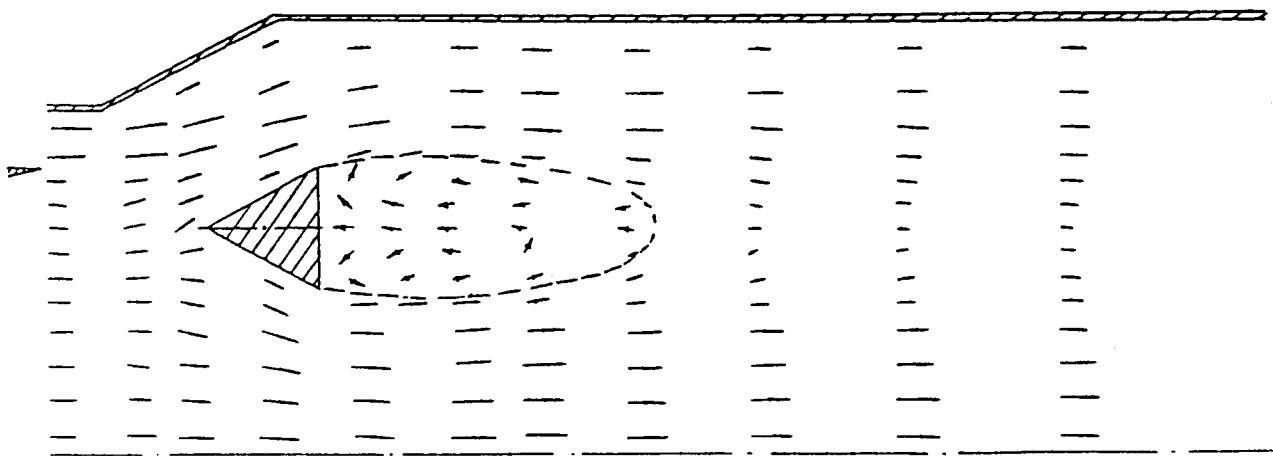


Figure 4. - Gas velocity vectors of a cold flow.

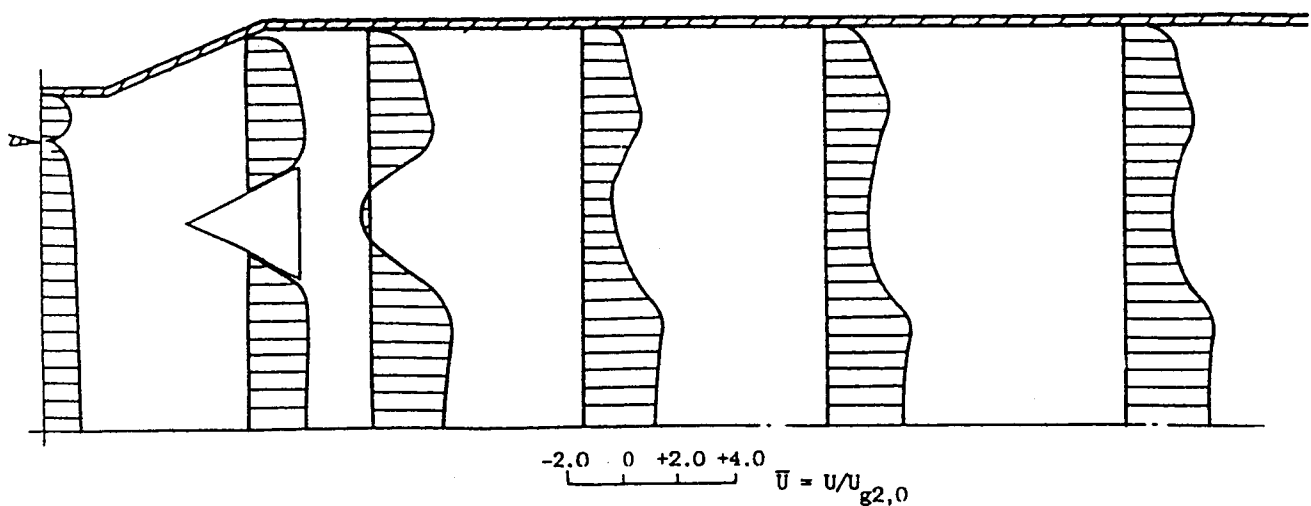


Figure 5. - X-Direction velocity component profiles in a gas flow.

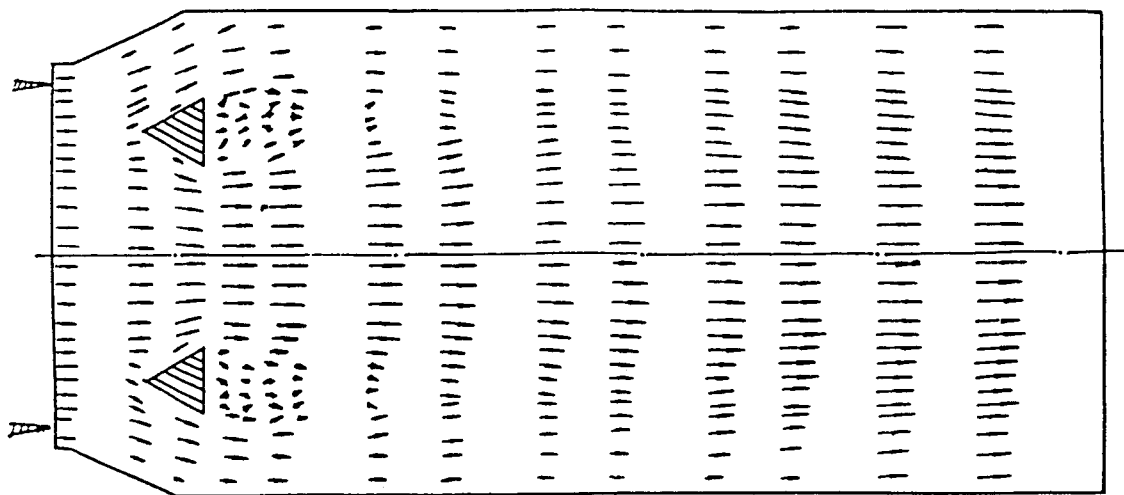


Figure 6. - Gas velocity vectors of a multiphase combustion flow.

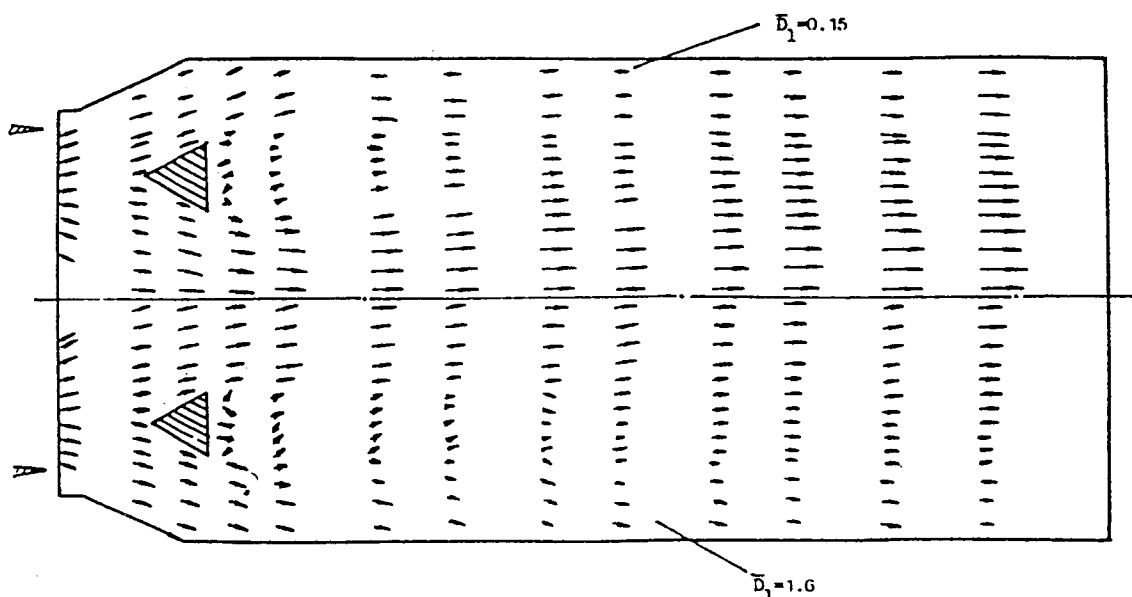


Figure 7. - Droplet velocity vectors of a multiphase combustion flow.

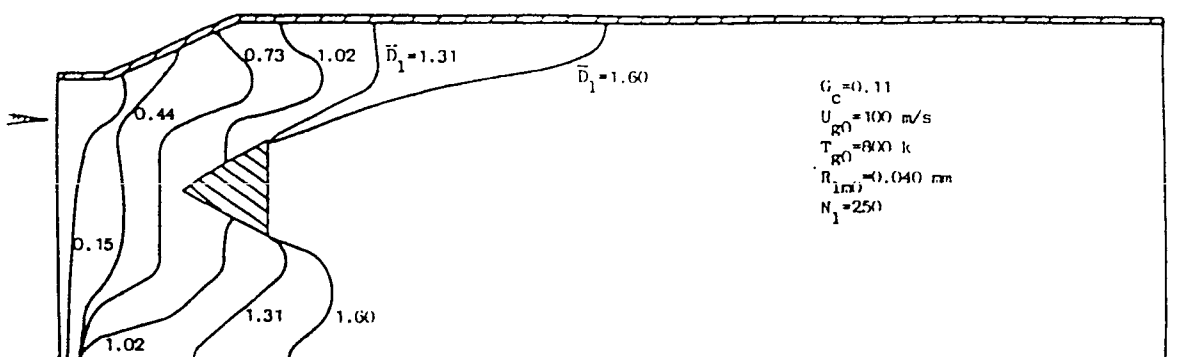
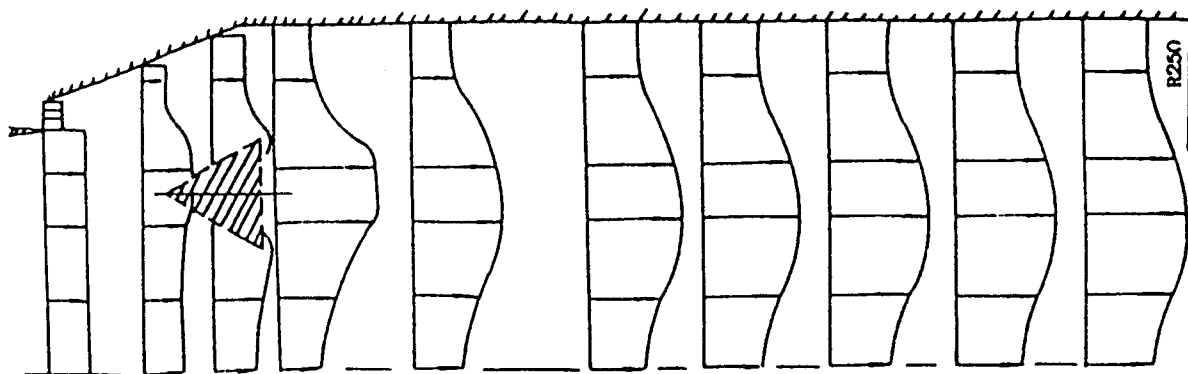
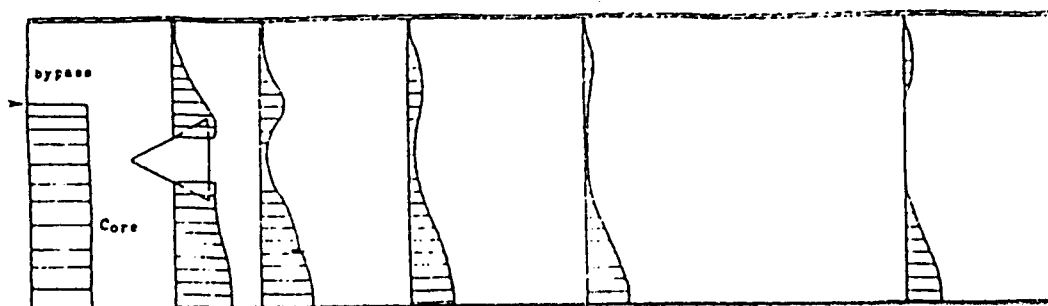


Figure 8. - Cascading vaporization of a multiphase spray flow.

ORIGINAL PAGE IS
OF POOR QUALITY



(a) Temperature field in a gas combustion flow.



(b) Gas fuel concentration field in a gas phase combustion flow.

Figure 9. - Gas phase combustion flow.

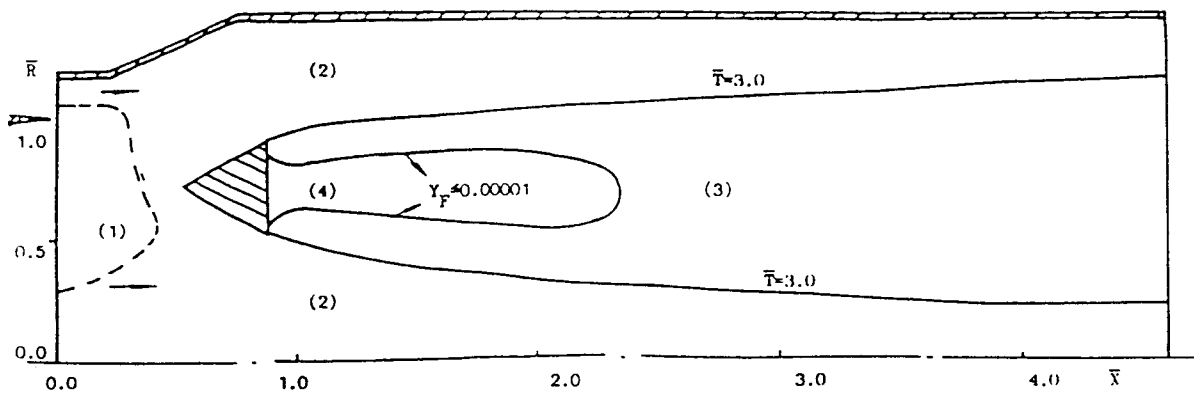


Figure 10. - Pre-evaporating flame mode. Droplet preheating and evaporating zone, (1); gas phase mixing zone, (2); gas phase burning zone, (3); fuel-deficient zone, (4).

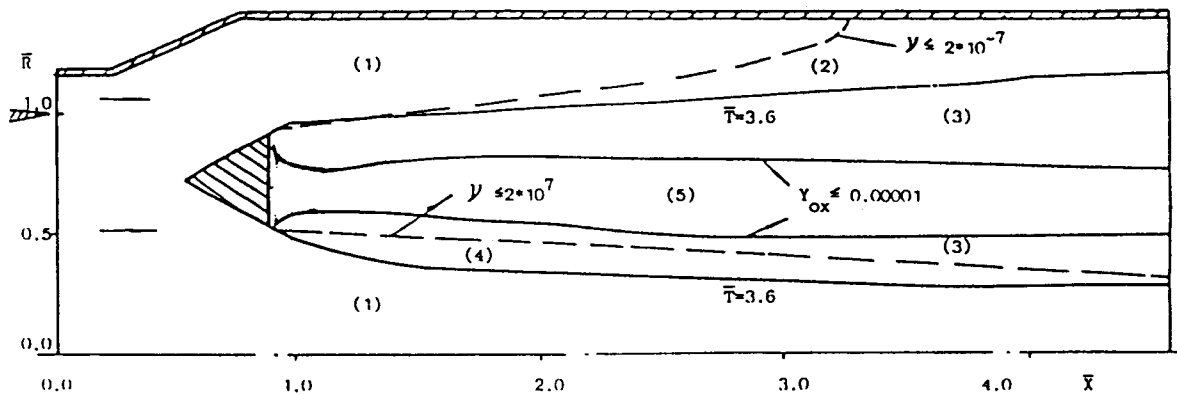


Figure 11. - Dense spray group flame mode. Droplet preheating and evaporating zone, (1); gas phase mixing zone, (2); gas phase burning zone, (3); gas phase and droplet burning zone, (4); oxygen-deficient zone, (5).

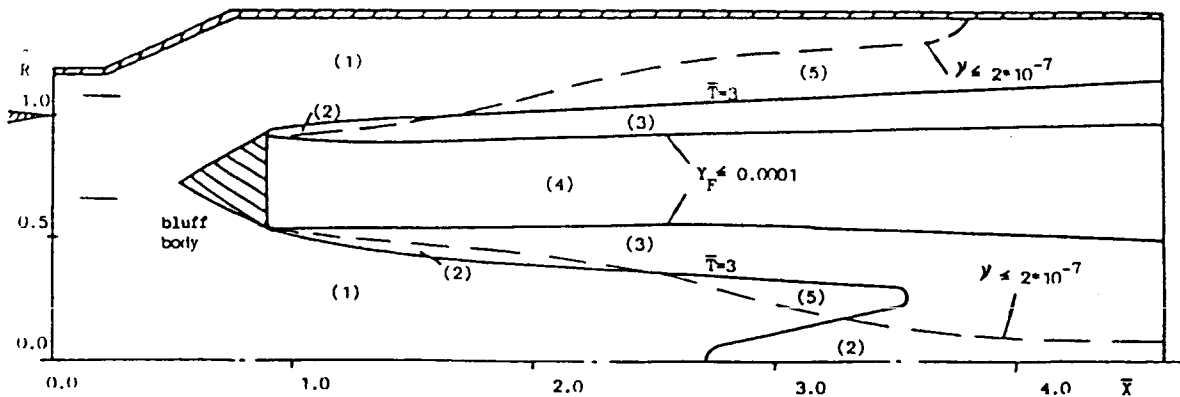
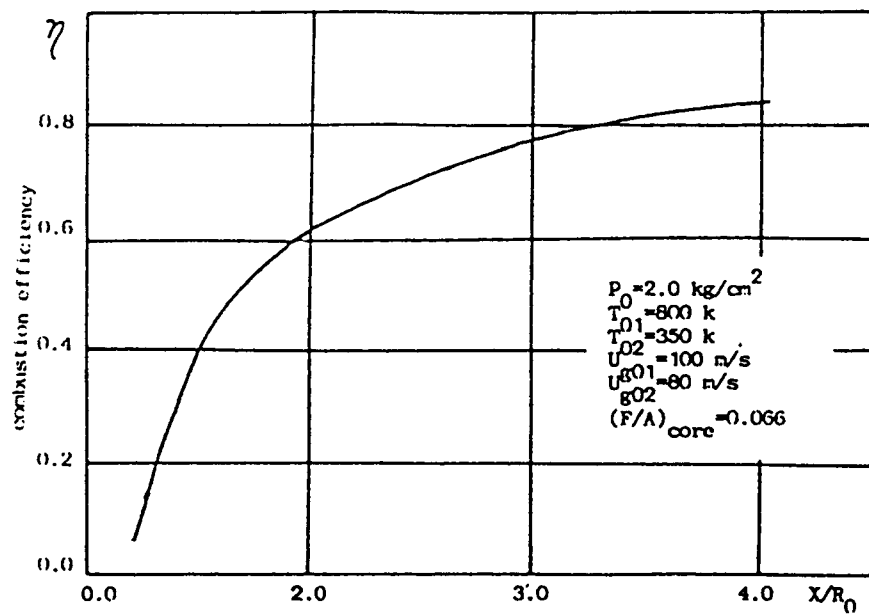
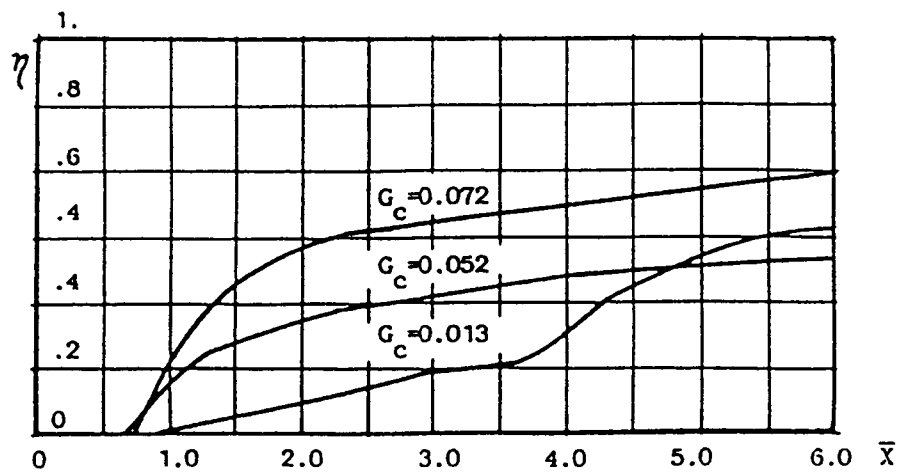


Figure 12. - Dilute spray group flame mode. Droplet preheating and evaporating zone, (1); gas phase and droplet burning zone, (2); gas phase combustion zone, (3); fuel-deficient zone, (4); gas phase mixing zone, (5).



(a) Gas phase flame.



(b) Multiphase flame.

Figure 13. - Axial distributions of combustion efficiency.

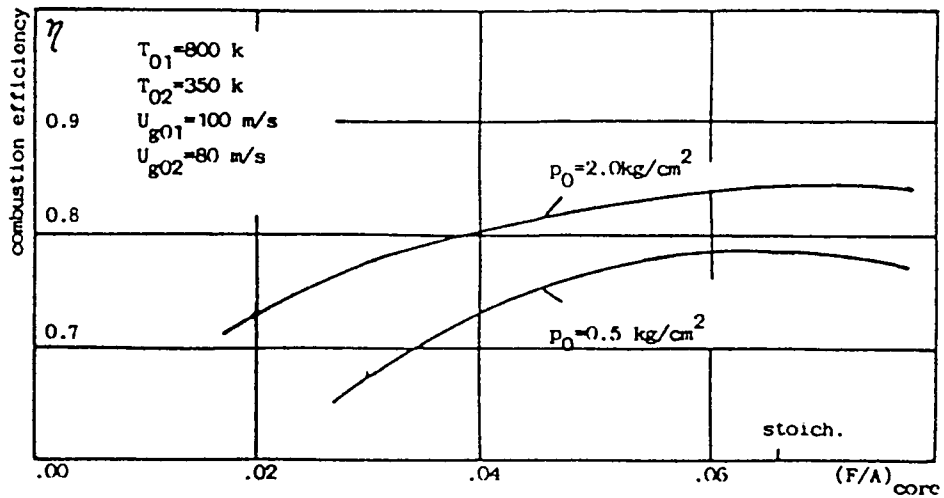


Figure 14. - Relation of gas phase combustion efficiency with fuel-air ratio and pressure.

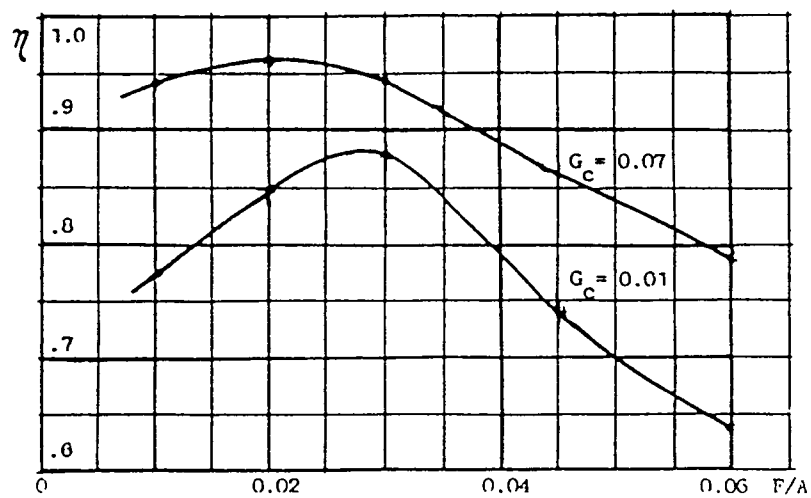


Figure 15. - Relation of multiphase combustion efficiency with fuel-air ratio and spray group combustion number.

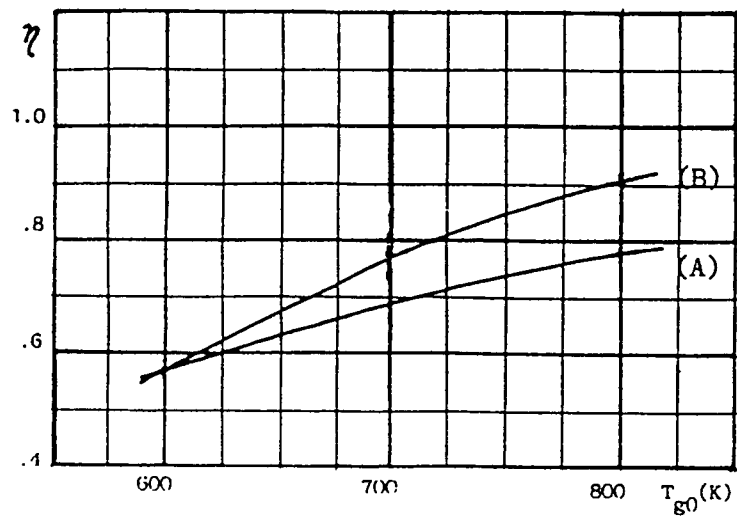


Figure 16. - Effect of inlet temperature on combustion efficiency. Gas phase flame, (A); multiphase flame (at better condition), (B).

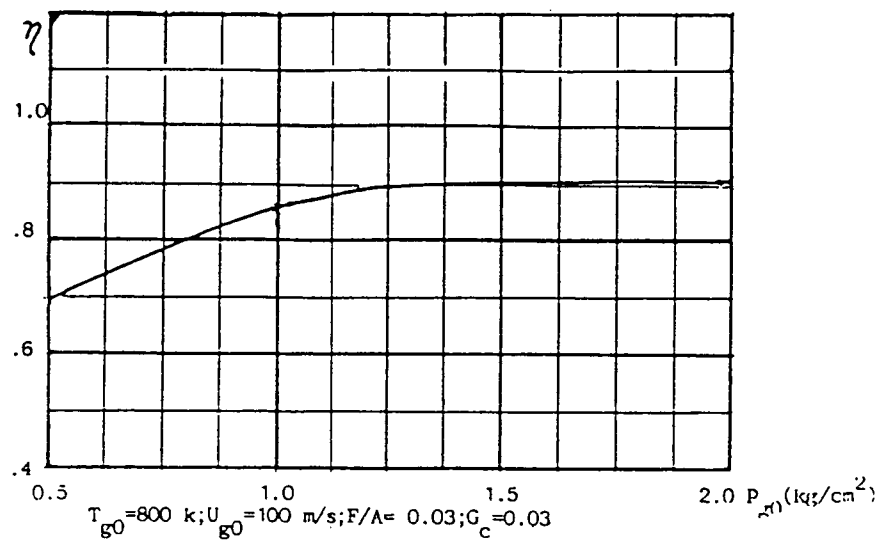


Figure 17. - Effect of inlet pressure on multiphase combustion efficiency.

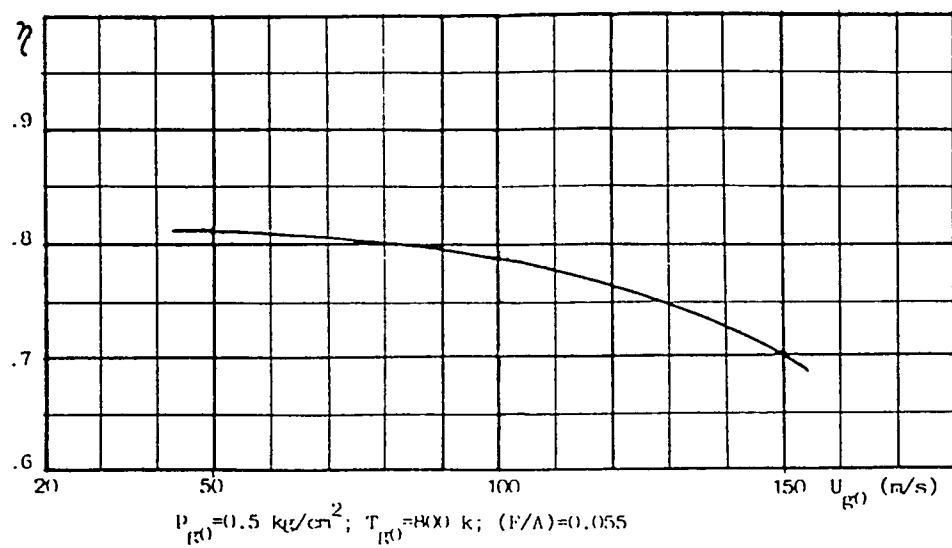


Figure 18. - Effect of inlet gas flow velocity on gas combustion efficiency.